JGR Space Physics

RESEARCH ARTICLE
10.1029/2020JA028108

Special Section:
Early results from the Global-scale Observations of the Limb and Disk (GOLD) mission

Observation of Postsunset OI 135.6 nm Radiance Enhancement Over South America by the GOLD Mission

Xuguang Cai[1], Alan G. Burns[1], Wenbin Wang[1], Liying Qian[1], Jing Liu[1], Stanley C. Solomon[1], Richard W. Eastes[2], Robert E. Daniell[3], Carlos R. Martinis[4], William E. McClintock[2], and Inez S. Batista[5]

[1]National Center for Atmospheric Research, High Altitude Observatory, Boulder, CO, USA, [2]Laboratory for Atmospheric and Space Physics, University of Colorado, Boulder, CO, USA, [3]Ionospheric Physics Consulting, Stoughton, MA, USA, [4]Center for Space Physics, Boston University, Boston, MA, USA, [5]Instituto Nacional de Pesquisas Espaciais, São José dos Campos, Brazil

Abstract The Global-scale Observation of Limb and Disk (GOLD) mission, for the first time, provides synoptic two-dimensional (2D) maps of OI 135.6 nm observations. These maps describe the unambiguous and dynamic evolution of nighttime ionospheric F_2-peak electron densities (N_mF_2) as the 135.6 nm airglow emission radiance correlates well with N_mF_2 at night. On November 19, 2018, the 135.6 nm radiance measured by GOLD, N_mF_2 measured by a digisonde, and GPS total electron content (TEC) measurements at Cachoeira Paulista (CP) all showed a postsunset enhancement, with an increase near 22:30 universal time. The 135.6 nm radiance map showed that this enhancement was due to the southward movement of the southern equatorial ionization anomaly (EIA) crest. Therefore, the GOLD observation showed the linkage between postsunset enhancement of N_mF_2 and EIA movement. Furthermore, unlike the southward movement of the southern crest, the corresponding EIA northern crest, however, did not show northward motion. This is the first time that the EIA hemispheric asymmetry, which included both different densities and movement of two crests in a short time period (<2-h), was captured. The cause of this asymmetric movement of the two crests is not clear and requires further investigation.

Plain Language Summary The postsunset enhancement of equatorial ionospheric N_mF_2 has been observed by low Earth orbit satellites and ground-based equipment. However, these observations can only provide variations along satellite orbits or at a single location. In this paper, we provide, for the first time, two-dimensional (2D) maps of nighttime OI 135.6 nm airglow observations by GOLD. These maps describe unambiguous and dynamic evolution of nighttime N_mF_2 as the 135.6 nm radiance is correlated well with nighttime N_mF_2. On the night of November 19, 2018, GOLD observed 135.6 nm radiance, N_mF_2 measured by digisonde, and total electron content at Cachoeira Paulista (CP) all exhibited a postsunset enhancement. This is the first time that the two dimensional (2D) measurements of the ionosphere by a geostationary satellite are compared with local observations in the same time range. The evolution of 135.6 nm radiance map suggests that this enhancement was mainly due to the southward movement of the southern equatorial ionization anomaly (EIA) crest. The corresponding northern EIA crest of CP is over the Ocean, which can be observed by GOLD and found to keep stationary, but not easily by other means of observations. This asymmetric movement of the two EIA crests is unknown and requires further investigation in the future.

Key Points:

- The GOLD nighttime observations match well with digisonde and total electron content at both single location and large area
- The observed postsunset OI 135.6 nm radiance enhancement at Cachoeira Paulista is due to the southward motion of southern Equatorial ionization anomaly (EIA) crest
- An event of EIA asymmetry motion occurred during the same time period (<2 h)

Correspondence to:
X. Cai,
xuguang@ucar.edu

Citation:
Cai, X., Burns, A. G., Wang, W., Qian, L., Liu, J., Solomon, S. C., et al. (2021). Observation of postsunset OI 135.6 nm radiance enhancement over South America by the GOLD mission. *Journal of Geophysical Research: Space Physics*, *126*, e2020JA028108. https://doi.org/10.1029/2020JA028108

Received 12 APR 2020
Accepted 21 NOV 2020

1. Introduction

The ionosphere F_2 layer has been studied for several decades, and many of its features are well known. During the nighttime, the F_2 layer electron density is expected to decay continuously due to the absence of photoionization by solar EUV radiation (Schunk & Nagy, 2009). However, sometimes the F_2 layer electron density does not decrease monotonically. Instead, it may increase and exhibit peak values after dark at certain locations in some local time ranges (19:00–23:00 or 1:00–5:00), which is referred to as the F_2 peak electron density nighttime enhancement (nighttime N_mF_2 enhancement). A number of observation studies have been carried out to investigate this nighttime electron density enhancement using data from ground-based ionosondes (Bellchambers & Piggott, 1958; Evans, 1965; Farelo et al., 2002; Jiang et al., 2016; L. Liu et al., 2013; Perna et al., 2014; Pezzopane et al., 2011; Y. Zhang et al., 2015; Zhao et al., 2008), incoherent

scatter radars (ISRs) (Mikhailov et al., 2000; Pavlov & Pavlova, 2005), total electron content (TEC) maps (Balan & Bailey, 1992; Balan & Rao, 1987; Balan et al., 1994; Davies et al., 1979; Essex & Klobuchar, 1980; Rajesh et al., 2016; Trivedi et al., 2013; Zhao et al., 2008), and Low Earth Orbiting (LEO) satellites (Y. Chen et al., 2015; He et al., 2009; Luan et al., 2008; Zhong et al., 2019). Many numerical simulation studies have also focused on the reproduction of the nighttime electron density enhancement (C. H. Chen et al., 2013, 2011; Le et al., 2014; Nicolls, et al., 2006; Ren et al., 2012; Thampi et al., 2011). Based on these numerous previous studies, it has been found that the nighttime N_mF_2 enhancement can be categorized into low latitude and mid-latitude ones from the perspective of geographic latitude. Furthermore, nighttime N_mF_2 enhancement can also be classified into postsunset and postmidnight enhancement. Farelo et al. (2002) gave a detailed description of the latitudinal and seasonal variations of nighttime N_mF_2 enhancement in mid-latitudes. Zhong et al. (2019) have provided a detailed explanation on the nighttime N_mF_2 enhancement in mid-latitudes for both ionosphere F_2 region and topside. They argued that the upward plasma motion due to neutral winds was the primary source of the nighttime enhancement in the ionosphere F_2 region.

Compared with many studies on the mid-latitude nighttime N_mF_2 enhancement, there are relative fewer studies focusing on low-latitude nighttime N_mF_2 enhancement. Anderson and Klobuchar (1983) suggested that the E × B drifts near the geomagnetic equator were responsible for the postsunset N_mF_2 enhancement between 19:00 and 23:00 local time (LT) over Ascension Island (7.95°S, 15°W; 15°S dip latitude), which is located equatorward of the southern crest of the equatorial ionization anomaly (EIA). Zhao et al. (2008) reported a postsunset N_mF_2 enhancement event in the Asia-Australian sector (June 28, 2002) and attributed it to the strong prereversal enhancement (PRE) of vertical plasma drifts near the geomagnetic equator based on the data from TEC maps, ionosondes and two LEO satellites. L. Liu et al. (2013) investigated a case of postmidnight N_mF_2 enhancement using data from a digisonde at Sanya (18.3°N, 109.6°E, dip latitude 8.44°N) and argued that the westward electric field played a major role in the formation of this enhancement. This case was further analyzed by Le et al. (2014) with a numerical model. They proposed that both neutral wind and westward electric field contributed to the reported postmidnight N_mF_2 enhancement in L. Liu et al. (2013). Y. Zhang et al. (2015) utilized four ionosondes in Japan to study the nighttime N_mF_2 enhancement and found that the postsunset enhancement was more frequent in summer months. Jiang et al. (2016) utilized four ionosondes in South China and Southeast Asia to study the latitudinal variation of low-latitude postmidnight N_mF_2 enhancement. They found that the LT of the occurrence of the postmidnight N_mF_2 enhancement was earlier in the geomagnetic southern hemisphere than the geomagnetic northern hemisphere.

Most of these previous studies of the low-latitude nighttime N_mF_2 enhancements were carried out using local observations such as ionosondes with only temporal variations. They rarely reported the ionosphere structure over a large area such as the corresponding nearby EIA structure. In reality, all these reported low-latitude nighttime N_mF_2 enhancements are near the geomagnetic equator or the EIA crests. Therefore, it is crucial to know the behavior of EIA structures over a large area when investigating the low-latitude nighttime N_mF_2 enhancements.

EIA is a phenomenon in the equatorial ionospheric F layer with two electron density crests at about ±15° magnetic latitudes and a density trough at the geomagnetic equator (Appleton, 1946). Due to different neutral wind and chemistry on the two sides of the geomagnetic equator, the densities on two crests are mostly different, which is called as EIA asymmetry. There are two types of EIA asymmetry. One is the hemispheric asymmetry, which is the density difference between the two crests in the same season. Another is the EIA annual asymmetry, which is the phenomenon that the December EIA strength is stronger than the June one. The asymmetry of EIA structures has been studied for decades by using data from multiple ionosondes (Thomas, 1968), TEC maps (Khadka et al., 2018; Rama Rao et al., 2006; M. L. Zhang et al., 2009; Zhao et al., 2009) and LEO satellites (Balan et al., 2013; Basu et al., 2009; Henderson et al., 2005; Huang et al., 2018; Kil et al., 2006; Lin et al., 2007; Luan et al., 2015; McDonald et al., 2008; Tallat et al., 2013; Tulasi Ram et al., 2009; Zeng et al., 2008). Zeng et al. (2008) found that the hemispherically asymmetric magnetic field was the most important factor to generate the EIA annual asymmetry. Khadka et al. (2018) investigated the EIA hemispheric asymmetry near 75°W near local sunset. They found that the asymmetry appeared more frequently in solstices and March equinox than September equinox. Tulasi Ram et al. (2009) found that the hemispheric asymmetry appeared near 12–13 LT during solstices. Dang et al. (2016) compared the role of

meridional neutral winds, photochemical effects, and magnetic field configuration played in the EIA hemispheric asymmetry in daytime during summer solstices. They suggested that the trans-equatorial neutral wind is a major contributor to the north-south asymmetry, which was similar to the modeling studies carried out by Balan et al. (2013).

It should be noted that all these previous studies focused on EIA asymmetry in a climatological way based on local ground observations and/or LEO satellite observations. LEO satellite observations can only provide cross-track scanned images or profiles at certain LTs near the orbit. These observations cannot delineate the spatial and temporal variability. TEC maps can provide both temporal and spatial variations of the EIA asymmetry with high resolution (as high as 1° × 1° and 5 min). However, most of the GPS receivers are located on continents (excluding the remote area such as Desert), which only counts for 30% of the Earth surface. Furthermore, the uneven distributions of the GPS receivers may also introduce errors

The newly launched NASA Global-scale Observation Limb and Disk (GOLD) mission, for the first time, provides two-dimensional (2D), synoptic maps of OI 135.6 nm airglow emission observations. These maps describe unambiguously the dynamic evolution of nighttime N_mF_2, since the 135.6 nm airglow emission rate correlates well with N_mF_2 at night (DeMajistre et al., 2004). They provide unambiguous observations of temporal and 2D spatial variations of the postsunset N_mF_2 enhancement over a large area that is not feasible in the aforementioned local observations, and thus advance our understanding of the nighttime electron density enhancement phenomenon.

In this paper, we focus on the postsunset N_mF_2/OI 135.6 nm radiance enhancement in low latitudes seen in 2D 135.6 nm airglow images obtained by GOLD. We report a case study of the postsunset N_mF_2 enhancement event at the Cachoeira Paulista (CP) station, Brazil (22.7°S, 45°W) (located in an area that is usually poleward of the southern crest of EIA) observed by GOLD on the night of November 19, 2018. In addition, we use TEC maps and digisonde data from the same area, which also observed a similar postsunset enhancement as GOLD did, to provide a comprehensive view of the phenomenon. The main purposes of this study are to validate the GOLD nighttime observation; provide new insight into the postsunset N_mF_2 enhancement and the motion of EIA crest, and demonstrate the powerful potential of GOLD observations.

2. Data Source

The GOLD instrument is onboard the SES-14 communication satellite, which was launched on January 25, 2018. The satellite is located in a geostationary orbit over 47.5°W. The only scientific instrument onboard is a Far Ultraviolet (FUV) imager, which has two similar and independent channels (Channels A and B) to perform airglow measurements (Eastes et al., 2017, 2019, 2020). Since GOLD makes measurements from the geostationary orbit, it is able to provide airglow images of the same region during the same time range every day (Cai et al., 2020a, 2020b; Karan et al., 2020; Laskar et al., 2020). At night, it observes the OI 135.6 nm with a spectral resolution of 0.04 nm. The data we utilize for this study are the GOLD Level 1C OI 135.6 nm radiance over the equatorial region in the South American continent between 21:55 universal time (UT) and 23:55 UT at local night. The nighttime OI 135.6 nm emission is produced mainly due to the recombination reaction between the oxygen ions (O^+) and electrons (McDonald et al., 2008; Rajesh et al., 2011). For the GOLD observation along a given line of sight (Kelley et al., 2003), it can be modeled as

$$B = \int_0^\infty \alpha N_e N_{o^+} ds \tag{1}$$

where B is the brightness of the emission, s is the line of sight distance, $\alpha = 7.3 \times 10^{-13} \times \left(1160 / T_e\right)^{0.5}$ is the recombination coefficient depending on electron temperature (T_e) (Meléndez-Alvira et al, 1999). N_e and $N_o{}^+$ are the number densities of electrons and O^+, respectively. In the F region, O^+ is the dominant ion species, and $N_o{}^+$ is approximately equal to N_e Thus, the observed radiance can be modeled as the integral of αN_e^2. Previous studies have demonstrated that OI 135.6 nm radiance exhibits similar variability to $N_mF_2^2$ (DeMajistre et al., 2004; Rajesh et al., 2011). Therefore, we can treat the airglow radiance and $N_mF_2^2$ as having the same variability in the following sections.

The critical frequency data of the F_2 layer (f_0F2) measured by the digisonde at CP were downloaded from the Global Ionospheric Radio Observatory (GIRO) web portal (Galkin et al, 2012; Reinisch & Galkin, 2011). The data are auto-scaled, and we checked every corresponding ionogram to ensure accuracy. N_mF_2 was derived from a relationship between the electron density and critical frequency $N_mF_2 = f_0F2^2 / 81$ (units of $/m^3$). The f_0F2 data have a 10-min temporal resolution.

The ionospheric TEC data with a 5-min temporal resolution and 1° spatial resolution (in both latitude and longitude) were obtained from the Madrigal database (Rideout & Coster, 2006). In order to match the resolution of GOLD nighttime observations, especially after 22:55 UT, we binned the TEC data with a 15-min resolution. Although TEC is the integration of electron density along the GPS path, it can be assumed that the TEC morphology is similar to that of N_mF_2, especially during solar minimum (Solomon et al., 2018). In addition, Rajesh et al. (2011) demonstrated that the OI 135.6 nm radiance had a linear relationship with the square of TEC (TEC^2). In the following, we use TEC^2, instead of TEC to compare with GOLD observation.

In order to extract the radiance at CP from the GOLD data, we calculated the average of the radiance in 1°, 2° and 5° diameter circular bins centered at CP. For the 1° bin, we collected all data points within a distance to CP (22.7°S, 45°W) less or equal to 0.5° of latitude and longitude. We then calculated the average of the radiance values in the bin. The distance to CP was increased to 1° and 2.5° when we utilized 2° and 5° bins, respectively. The 1° bin is adapted to match the spatial resolution of the TEC data so that a direct comparison can be carried out. We checked the skymap of the digisonde at CP from the drift database of GIRO, and found that the horizontal scale of the digisonde measurements is in a circle with a maximum radius of 110 km (~1°). Therefore, the 2° bin was employed for comparison with the digisonde measurements. Finally, we added the 5° bin because sometimes the GOLD measurements in the nighttime may have high noise levels; a larger bin size improves signal-to-noise level and ensures data quality.

On the night of November 19, 2018, GOLD began to image the regions of West Africa and the Atlantic Ocean using Channel B from 20:10 UT. It imaged both the northern and southern hemispheres every 15 min in turn (for example, at 20:10 UT, GOLD imaged the northern hemisphere near west Africa, then the southern hemisphere at 20:25 UT and again the northern hemisphere at 20:40 UT. The region that was imaged was moving westward due to the movement of the day night line). Channel B of the FUV imager began to image South America from 21:55 UT, and then at 22:25 UT, and again from 22:55 UT to 23:55 UT with a 15-min cadence. Between 23:10 UT and 23:55 UT, Channel A started to image the northern hemisphere simultaneously with Channel B. In a word, the temporal resolution is 30-min from 20:10 to 22:55 UT, and 15-min between 23:10 and 23:55 UT. The spatial resolution of the measured OI 135.6 radiance varies from geomagnetic equator to EIA crests, but mostly between 0.5° × 0.5° and 1° × 1°. The nighttime OI 135.6 nm radiance measurement error is around 10% (McClintock et al., 2020). We have four images covering both the northern and southern hemispheres in that time period, which provided the 2D evolution of the nighttime equatorial ionosphere.

3. Observation Results

3.1. Observations over Cachoeira Paulista

Figure 1a shows the variations of the airglow radiance at CP measured by GOLD and the corresponding variations of $N_mF_2^2$ derived from f_0F2 measured by the digisonde at CP between 22:25 and 23:55 UT on November 19, 2018. GOLD first scanned CP at 22:25 UT, and then again at 22:55 UT. From 22:55 to 23:55 UT, GOLD channel B scanned the southern hemisphere every 15 min, so we have GOLD data at CP at 23:10, 23:25, 23:40, and 23:55 UT. The comparison between GOLD and local observations over a single location has great advantages over previous comparisons of monthly climatology provided by LEO satellites because much variability can be removed by doing monthly climatology, such as the comparison between Constellation Observing System for Meteorology, Ionosphere, and Climate and ionosonde measurements in Lei et al. (2007). In addition, the GOLD measurements are 2D synoptic maps, providing information over a much larger area, which is not available from LEO cross-track scanning. When binned at 1° (black dots), the radiance increased from 12.5 Rayleigh at 22:25 to 33.13 Rayleigh at 23:25 UT, and then decreased to 23.74 Rayleigh at 23:55 UT. The 2° binned radiance (blue dots) increased from 12.7 Rayleigh at 22:25 to 31.02 Rayleigh at 23:40 UT, and then decreased to 27.72 Rayleigh at 23:55 UT. The 5° binned radiance

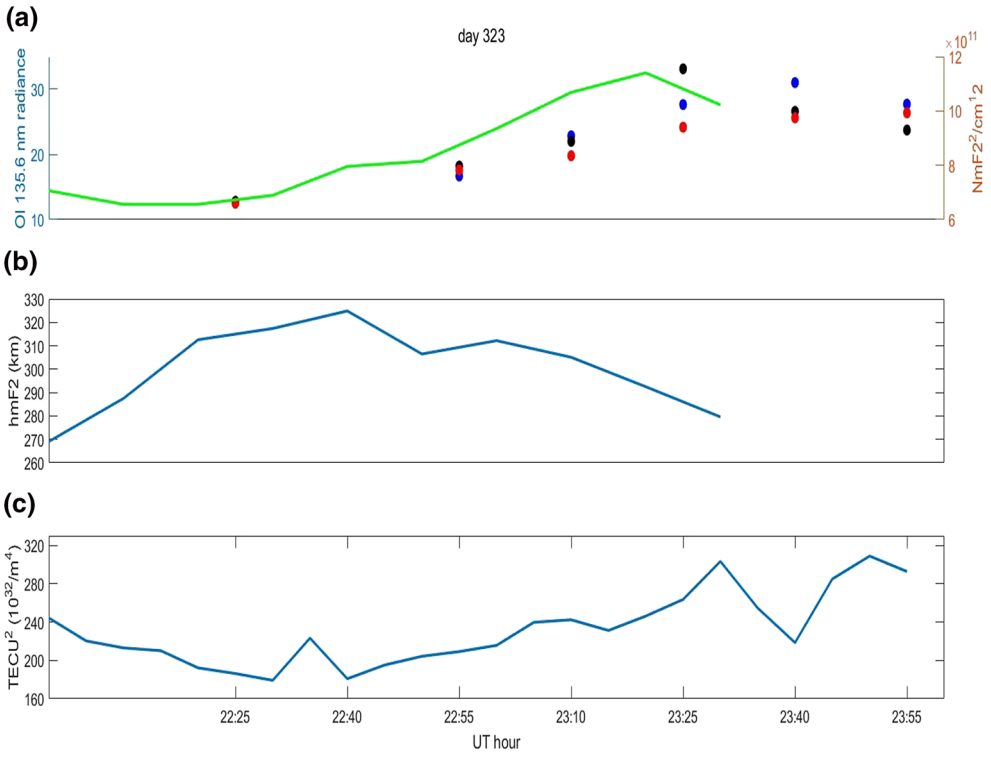

Figure 1. (a) The GOLD measured OI 135.6 nm radiance at CP averaged in 1° bin (black point), 2° bin (blue point) and 5° bin (red point), and the NmF_2^2 of digisonde at (green line) on November 19, 2018; (b) the digisonde measured h_mF_2 at CP and (c) the TEC^2 at CP.

(red dots) increased from 12.8 Rayleigh at 22:25 to 26.38 Rayleigh at 23:55 UT. GOLD radiance data in all bins are with good quality and high signal-to-noise ratios. $N_mF_2^2$ measured by the digisonde increased from 6.56×10^{11} / cm^6 at 22:20 UT to 1.14×10^{12} / cm^6 at 23:20 UT, and then decreased to 1.02×10^{12} / cm^6 at 23:30 UT. There was no $N_mF_2^2$ available after 23:30 UT because spread F appeared at CP (see Figure A1 in Appendix A), which prevents the observation of f_0F_2. With the detailed variations of radiance from three bin sizes presented, we found that the 1° and 2° binning results were closer to the variation of $N_mF_2^2$ compared with the 5° binning. This is because the results with a larger bin size can be influenced more easily by changes in the areas further away from the center (CP).

The corresponding h_mF_2 is shown in Figure 1b. It increased from 269 km at 22:00 UT to 325 km at 22:40 UT, and then decreased to 293 km after 22:50 UT. There was a small increase of h_mF_2 at 23:00 UT, but it decreased with time after that. In addition, we also present the corresponding TEC^2 at CP (from the 1° binned Madrigal data containing the CP site) in Figure 1c. Although TEC^2 had a fluctuation from 22:30 to 22:40 UT, it increased from 186.3 $TECU^2$ at 22:25 to 303.5 $TECU^2$ at 23:30 UT, and then decreased to 218.4 $TECU^2$ at 23:40 UT, and again increased to 308.7 $TECU^2$ at 23:50 UT. This variation was close to that of 1° binning results of OI 135.6 nm radiance (increasing from 22:25 to 23:25 UT, and then decreasing until 23:55 UT) mentioned earlier. Based on above description and comparison, the temporal variation of the GOLD observed OI 135.6 nm radiance over CP on November 19, 2018 correlated well with the corresponding $N_mF_2^2$ measured by the digisonde and TEC^2 measured by GPS receivers and thus can be used to track the nighttime ionospheric $N_mF_2^2$ variations.

We further compared the variations of OI 135.6 nm radiance over CP with the corresponding $N_mF_2^2$ and TEC^2 in the whole November, and carried out a correlation analysis for the month between OI 135.6 nm airglow intensity and $TEC^2/N_mF_2^2$ for the same UT. The correlation coefficient between OI 135.6 nm and $N_mF_2^2$ are 0.8685 at 22:25 UT, 0.9192 at 22:55 UT, 0.9324 at 23:10 UT, 0.8945 at 23:25 UT, 0.8472 at 23:40 UT, and 0.8391 at 23:55 UT, respectively. The correlation coefficients between OI 135.6 nm and TEC^2 at these UTs

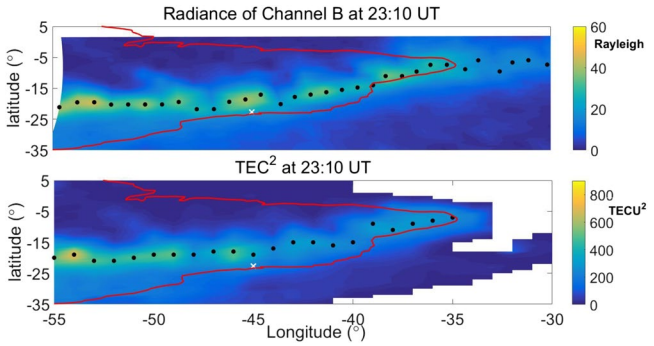

Figure 2. Latitude-longitude distribution of GOLD measured OI 135.6 nm radiance (top) and the TEC^2 map (bottom) at 23:10 UT. The white cross marked the location of CP (22.7°S, 45°W). The red line marked the coastline of South American continent, and the black points are the locations of the EIA southern crest peak. The white area on both maps stand for the area that is not covered by GOLD and GPS receivers' network.

are 0.9168, 0.8545, 0.8283, 0.8227, 0.8464, and 0.8668, respectively. All are above 0.8. This demonstrates that the OI 135.6 nm and the N_mF_2 and TEC^2 are correlated well in 2018 November. More comparisons between GOLD and local observation in other months in the same time range will be carried out as future work (Cai et al., 2020b).

3.2. GOLD and TEC Observation over South American Continent

After showing the comparisons of GOLD, digisonde, and TEC data at a single location, we turn to the observations over a large area. Figure 2 shows an example of the comparison between the TEC^2 map and GOLD radiance map in the South American sector (coast-line shape marked in red) at 23:10 UT. The location of CP is marked on both maps (white cross). The spatial resolution of the airglow radiance and TEC data is 1°, and both of them have been processed by a moving window of 5° along each latitude to remove the small-scale perturbations on the EIA crests. We also marked the location of the peak density of the southern EIA crests in both maps (black dots). The distance in latitude between CP and the corresponding peak of the southern crest in the GOLD map was 4.1°, and 3.7° in the TEC^2 map, with a difference of less than 1°. The locations of the peaks of the southern EIA crest in both two maps were close to each other, apart from several longitudes (such as 47°W and 39°W). It should be noted that the peak location on TEC^2 map is not available outside of the continent due to the TEC data unavailability over the Ocean. In all, the nighttime GOLD observations match well with the observation made by other instruments in both single locations and over a large area.

Figure 3 shows the airglow radiance in the South American sector (35°S to 5°N and 30°W to 70°W) imaged by GOLD Channel B from 22:25 to 23:55 UT, with both CP (white cross) and the corresponding location of the southern crest EIA peak at 45°W (black dot) marked on. At 22:25 UT, CP was poleward the EIA southern crest and had a distance of 7.4° from the peak of the southern EIA crest at 45°W. At 22:55 and 23:10 UT, the south crest was moving southward toward CP, and the distance between CP and the peak at 45°W decreased to 4.9° and 4.1°, respectively. As the EIA southern crest moved closer to CP after 22:25 UT, N_mF_2 at CP increased from 22:30 UT, as shown in Figure 1b. At 23:25 UT, the southern crest peak was 3.3° north from CP. At 23:40 UT, the southern crest was almost over CP (with a distance of only 0.2°). The peak was finally passed over CP and located 0.6° south of CP at 23:55 UT. Therefore, based on the dynamic evolution of the GOLD 135.6 nm radiance map shown in Figure 3, we can see that the postsunset enhancement of

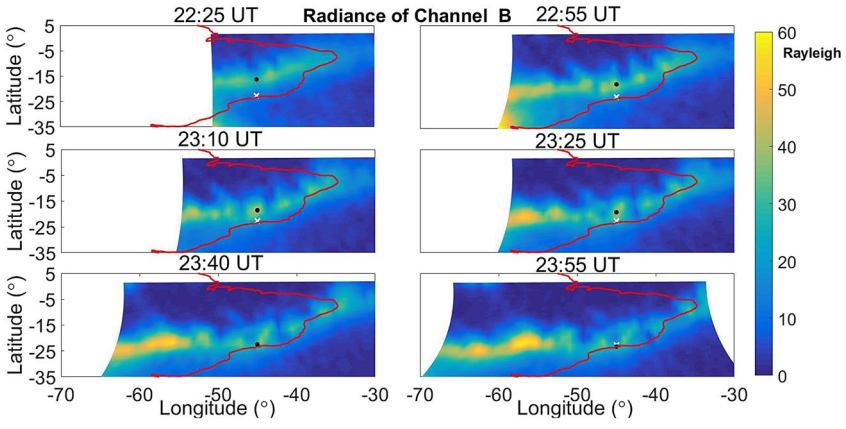

Figure 3. The latitude-longitude distribution of the OI 135.6 nm radiance measured by GOLD Channel B from 22:25 to 23:55 UT (22:25, 22:55, 23:10, 23:25, 23:40 and 23:55) on Nov 19, 2018. The white cross in each subplot marked the location of CP (22.7°S, 45°W), and the black point is the location of EIA southern crest peak at 45°W. The red line marked the coastline of South America continent. The white area on each subplot stand for the area that is not scanned by GOLD.

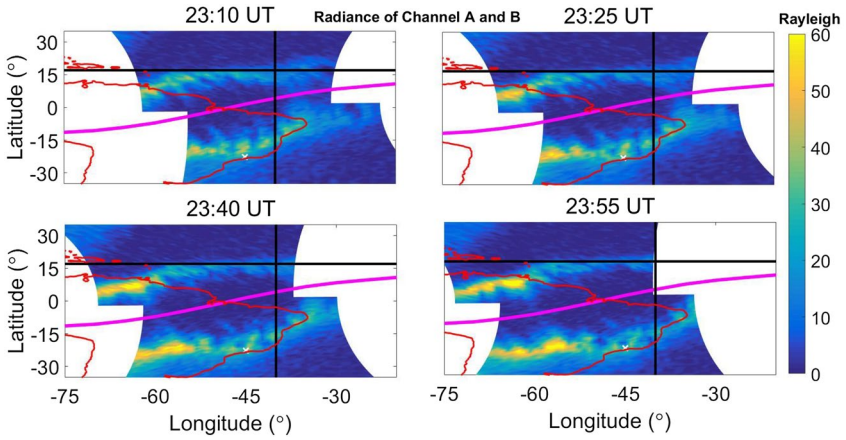

Figure 4. The longitude-latitude distribution of OI 135.6 nm radiance from Channel A and Channel B between 23:10 and 23:55 UT with a temporal resolution of 15 min. The pink line is the geomagnetic equator. Blacked horizontal line marked 18°N and vertical line marked 40°W. The white cross marked the location of CP (22.7°S, 45°W). The red line marked the coastline of South and central America continent.

airglow radiance/N_mF_2 observed at CP is a part of the poleward movement of the southern EIA crest. They revealed clearly that the southward movement of the southern EIA crest resulted in the postsunset enhancement in GOLD airglow radiance, digisonde N_mF_2 and GPS receiver TEC at CP. Therefore, the postsunset enhancement of N_mF_2/OI 135.6 radiance is due to spatial variation of EIA. This is different from the previous explanations that the PRE near the geomagnetic equator caused the postsunset of N_mF_2 in low latitude ionosphere (Anderson & Klobuchar, 1983; Zhao et al., 2008). In other words, it is the spatial variations of EIA that directly cause this postsunset enhancement of N_mF_2/OI 135.6 radiance, not the temporal variation of E × B drift. The linkage between the postsunset enhancement of N_mF_2 and the EIA crest movement in a short time period is discovered. This new finding will enhance the understanding of nighttime equatorial ionosphere and help avoid possible misinterpretation obtained from single local ground observation. More similar cases are searched for and will be studied in the future.

Two-dimensional images from GOLD not only provide the evolution of the EIA southern crest, but also provides the behavior of the EIA northern crest simultaneously from 23:10 UT. Figure 4 presents the OI 135.6 nm radiance images by both Channel A and Channel B from 23:10 UT to 23:55 UT with the coastline of continent marked on. Unlike the 5° poleward motion of the southern EIA crest, the northern crest moved much less poleward between 23:10 UT and 23:55 UT. To the east of 40°W, the northern EIA crest did not even move, when compared with the 18°N line during this time period. On the other hand, the distance between the two crests between 40°W and 50°W was increasing during the same time period. For example, at 23:10 UT, the distance between the two EIA crests near 45°W was around 35.6° in latitude, and it increased to 41.1° at 23:55 UT. Therefore, the meridional movement of the two EIA crests showed hemispheric asymmetry. For the corresponding TEC map, it cannot show the variation like GOLD OI 135.6 nm map did due to the difficulty to situate GPS receivers in the Ocean and remote area. The hemispherically asymmetric movement of the EIA can only be captured by GOLD in this region because the scanning from the geostationary orbit is not restricted by surface conditions. Unlike those previous studies about EIA asymmetry that only reported and simulated the climatological electron density difference of EIA crests (Dang et al., 2016; Luan et al., 2015; Tulasi Ram et al., 2009), GOLD observations here capture the process of asymmetric motion of two EIA crests in a short time period (<2 h). This again demonstrates the powerful capacity and advantages of the GOLD 2D OI 135.6 nm radiance map.

3.3. Other Related Local Observations

We checked the ionograms during the same time period at two stations near the geomagnetic equator: Sao Luis (2.6°S, 45°W) and Fortaleza (3.9°S, 38.4°W). Spread F occurred over both stations between 22:00 UT and 23:50 UT (see Figures A2 and A3 in Appendix A), indicating the unavailability of $N_mF_2^2$ data. We then

checked the vertical ion drift velocity (VID) from the digisonde at CP on November 19, 2018, as shown in Figure 5. It was upward with a maximum magnitude of 20 m/s before 22:50 UT and then changed to downward after 23:00 UT, which matched well with the variations of h_mF_2 and $N_mF_2^2$ in Figure 1. When there was upward VID, h_mF_2 moved upward whereas it decreased with downward VID. By looking at the VID at CP during this time period on other days in November 2018 without such a postsunset N_mF_2 enhancement occurring at CP, we found downward VID or an upward one with a much smaller value (<10 m/s) or a combination of both. The magnitude of VID at CP on November 19 was the largest during the whole month from 22:30 to 23:00 UT. All this information suggests that there existed large southward and upward ion drifts in the southern EIA crest on November 19th from about 42°W to 53°W. For the corresponding northern crest, there were two digisondes nearby. One is in Boa Vista (2.8°N, 60°W), another is in Belem (1.43°N, 48.44°W). Unfortunately, the digisonde at Belem did not have observation on this day. The digisonde at Boa Vista only observed spread F after 23:10 UT, suggesting the unavailability of N_mF_2 and vertical ion drift results.

3.4. Geomagnetic Activity

Figure 6 presents the geomagnetic activity index (Kp), Auroral electrojet (AE) index, Disturbance storm time index (Dst), and F10.7 variations between November 17 and 20 in 2018. The temporal resolution of Kp, Dst, and F10.7 are all one hour (from https://omniweb.gsfc.nasa.gov/form/dx1.html). The AE was in 1-min resolution and smoothed by a 10-min moving window. For AE, we set AE<250 nT as geomagnetic quiet time. As shown in Figure 6a, AE was <250 nT before 15 UT on November 19. It increased from 15 UT on November 19 and reached a maximum of 545 nT around 20 UT. Then it fluctuated around 400 nT during the rest of November 19, 2018. Kp increased from 0.3 to 1.7 on this day. F10.7 was 69 during this period with little fluctuations, suggesting minor roles of F10.7 variations on the ionosphere during these days. Dst had a minimum of −7 nT on November 19, 2018. From the geomagnetic indices shown in Figure 6, there was a weak geomagnetic disturbance beginning from 15 UT on November 19, 2018.

4. Discussion

Based on the observation results in previous sections, it is found that this observed postsunset enhancement is due to the southward motion of EIA southern crest. However, the corresponding EIA northern crest with weaker density did not move northward. In the following, the formation mechanism of this special EIA asymmetric movement is explored.

We ran the National Center for Atmospheric Research (NCAR) Thermosphere-Ionosphere-Electrodynamics General Circulation Model (TIE-GCM) (Richmond et al., 1992; Roble et al., 1988) with a resolution of 2.5° × 2.5° × 1/4 scale height for this observed postsunset enhancement event and the asymmetry movement of the crests on November 19, 2018. Unfortunately, the TIE-GCM with the high-latitude input of either Heelis (Heelis et al., 1982) or Weimer (Weimer et al., 2005) could not reproduce this observed southward movement feature of the southern crest. Therefore, our explanation has to be based on the current available observations only.

From the geomagnetic activity shown in Figure 6, there might also be effects of penetration electric fields on the ionosphere in low-latitudes (Wang et al., 2008). However, we found that in the most of the days in November 2018, the EIA crests did not exhibit hemispherically asymmetric movement as they did on November 19 between 22:25 and 23:55 UT, even with stronger geomagnetic disturbances. Figure A4 shows geomagnetic activity from November 4 to November 6, 2018. From the AE index shown in Figure A4, AE also increased around 15 UT on November 4, which is similar to its behavior on November 19. However, with that strong AE in this geomagnetic storm, the corresponding EIA structure (Figure A5) did not exhibit the asymmetry movement observed on November 19. Therefore, the geomagnetic activity influence on this EIA asymmetric movement is apparently weak.

As shown in Figure 3, the southern EIA crest was approaching CP (but had not passed it) from 22:25 UT to 23:25 UT. The magnitude of the crest at 45°W increased from 28.4 Rayleigh at 22:25 UT to 40.3 at 23:25 UT. Furthermore, the magnitude of OI 135.6 nm airglow emission over CP also increased during this time period. Based on Su et al. (1994), the postsunset enhancement of N_mF_2 was attributed to the strong equatorial

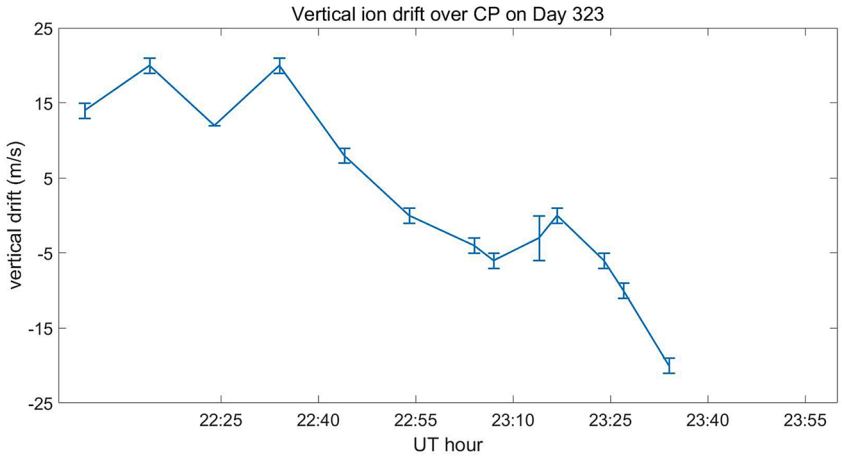

Figure 5. Vertical ion drift velocity and error bar at CP between 22:00 and 23:50 UT on November 19, 2018 (DOY 323). The time resolution is 10 min. The UT time marked on *x*-axis matches with the time when GOLD Channel B scanned over CP (22:25 to 23:55 UT). CP, Cachoeira Paulista; GOLD, Global-scale Observation of Limb and Disk.

PRE. Therefore, the E × B drifts over the geomagnetic equator should play a role in this observed postsunset enhancement of N_mF_2 or OI 135.6 nm radiance. It should be noted the E × B drifts over the geomagnetic equator should have the same impact on both sides of the equator (Chen & Lei, 2019; Eccles et al., 2015), namely the two crests should exhibit the same behavior. However, the two crests of the EIA actually exhibited asymmetric movement. Unlike the poleward movement and the enhancement of the southern crest near CP, the northern crest did not move poleward and there was also no apparent enhancement of the magnitude. Therefore, the E × B drifts should not be the only reason for this asymmetric movement of EIA crests. The behavior of electron density in the ionosphere F_2 region is determined by chemistry, E × B transport, neutral wind transport and ambipolar diffusion (e.g., J. Liu et al., 2016). Apart from E × B drifts, the other three terms could also contribute to this asymmetric movement. It should be noted that GOLD nighttime observations can only provide N_mF_2, not hmF_2. It is possible that the hmF_2 of the northern and southern crests are different, causing different recombination effects. Ambipolar diffusion depends on gravity and the ion/electron pressure gradient force. The latter includes the ion/electron density and plasma temperature (Lei et al., 2008). It tends to react to the changes caused by other physical processes. It is possible that the plasma temperatures in the two crests are different, causing different ambipolar diffusion. There is also a feedback effect insofar as the occurrence of a different density in each hemisphere then changes ambipolar diffusion. Balan et al. (2013) discussed how the geomagnetic meridional winds can plays an important role in the formation of north-south asymmetries:

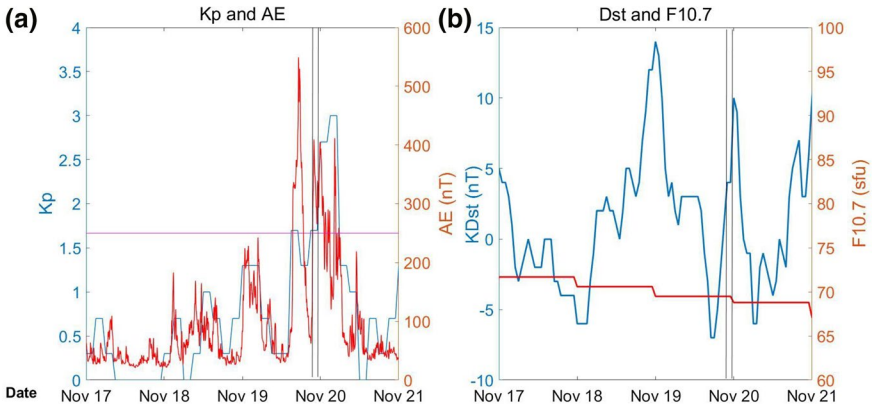

Figure 6. Temporal variation of (a) Kp and AE, and (b) F10.7 and Dst between Nov 17 and 21 in 2018. The pink line stands for AE = 250 nT. AE, Auroral electrojet; Dst, Disturbance storm time.

$$U_{nm} = V \cos D + U \sin D \quad (2)$$

where U and V stand for the zonal and meridional neutral winds, and D represents the declination angle of the Earth's magnetic field. Equation 2 also suggests that the direction of the second term on the right-hand side is determined by both the declination angle and zonal wind, while the direction of the first term on the right-hand side is determined by the meridional wind only. The magnetic declination angle, from the International Geomagnetic Reference Field (IGRF) model (Finlay et al., 2010), has both positive and negative values between 0° and 60°W, where the variation of the geomagnetic equator is also the strongest. In addition, in November, meridional winds blow northward from the southern hemisphere to the northern hemisphere due to the increased pressure gradient between the two hemispheres (generated by different solar zenith angles). The northward meridional wind pushes the ions along the field line toward the geomagnetic equator to higher altitudes, generating less recombination in the southern hemisphere. While it pushed the ions away from the geomagnetic equator to lower altitudes, resulting in more recombination in the southern hemisphere. Neutral wind transport may also create a suitable foundation and precondition for the asymmetric movement. Regarding the chemistry, molecular nitrogen (N_2) near the F_2 region dominates the chemical recombination process during nighttime. As mentioned earlier, the behavior of E × B drifts and neutral wind transport can also modulate the chemical loss by transporting plasma to higher or low altitudes.

The EIA asymmetric movement reported in this paper is a specific space weather event, which may require a more accurate description of the thermosphere and ionosphere state and its variations during the event before it can be properly understood. Further investigation of this phenomenon with more observations and numerical simulations are needed.

5. Conclusions

In summary, we report a postsunset OI 135.6 nm radiance/N_mF_2 enhancement over CP (a location normally south of the southern EIA crest) observed by GOLD, digisonde, and TEC. Further analysis of GOLD images leads to the discovery of a special EIA asymmetry event. Our main findings are summarized as follows:

1. It is the first time that the 2D synoptic measurements from a geostationary satellite are compared with the corresponding local observations (digisonde and GPS receiver) during the same time period (22:25–23:55 UT). The comparison is reasonably good in both single location (CP) and over a large area (South American continent)
2. The dynamic evolution of the 2D OI 135.6 nm radiance observed by GOLD revealed that the postsunset enhancement at CP was caused by the southward movement of the southern EIA crest that passed over CP. The EIA southern crest moved 5° southward between 22:25 and 23:55 UT. Therefore, it was a result of a spatial variation instead of a local temporal variation. This is different from the explanation provided by previous observational studies, which is the postsunset enhancement of E × B drift. This finding provides new insight into the postsunset enhancement of N_mF_2 in the low latitude ionosphere
3. The corresponding EIA northern crest did not show such apparent motion during the same time range, indicating asymmetric movement of EIA crests. Compared with previous studies of climatological EIA asymmetry, this EIA asymmetric movement occurring in a short time (<2-h) includes not only different plasma densities but also different motions. And it can only be captured by GOLD due to the difficulty in situating the local observation equipment in the ocean and remote area of the continent
4. The detailed mechanism of this EIA asymmetric movement is still unknown, but shall be the combination of chemistry, E × B transport, neutral wind transport and ambipolar diffusion. The geomagnetic activity may play minor roles

Further understanding relies on future observational and theoretical studies. More equipment such as Fabry-Perot interferometer (FPI) (measuring neutral wind around 250 km altitude) and meteor radars (measuring neutral wind between 80 and 100 km altitudes) are needed in this area to know the behavior of neutral

wind. On the other hand, numerical models with improved descriptions of geomagnetic activity and low atmosphere forcing to better reflect the ionosphere daily conditions are also necessary.

Appendix A: Figures

Figure A1 shows the Ionograms between 22:00 UT and 23:50 UT at Cachoeira Paulista (CP) (22.7°S, 45°W) on November 19, 2018 (DOY 323) from digisonde.

Figure A2 shows the Ionograms between 22:00 UT and 23:50 UT at Sao Luis, Brazil (2.5°S, 44.2°W) on November 19, 2018 (DOY 323) from digisonde.

Figure A3 shows the Ionograms between 22:00 UT and 23:50 UT at Fortazela (3.7°S, 38.5°W) on November 19, 2018 (DOY 323) from digisonde.

Figure A4 shows temporal variation of Kp and AE (left panel), Dst and F10.7 (right panel) between Nov 3 and 7 in 2018. The pink line stands for AE = 250 nT. AE, Auroral electrojet; Dst, Disturbance storm time.

Figure A5 shows the longitude-latitude distribution of OI 135.6 nm radiance from Channel A and Channel B between 23:10 and 23:55 UT with a temporal resolution of 15 min on November 4, 2018 (DOY 308). The pink line is the geomagnetic equator. Blacked horizontal line marked 18°N and vertical line marked 40°W. The red line marked the coastline of South and central America continent.

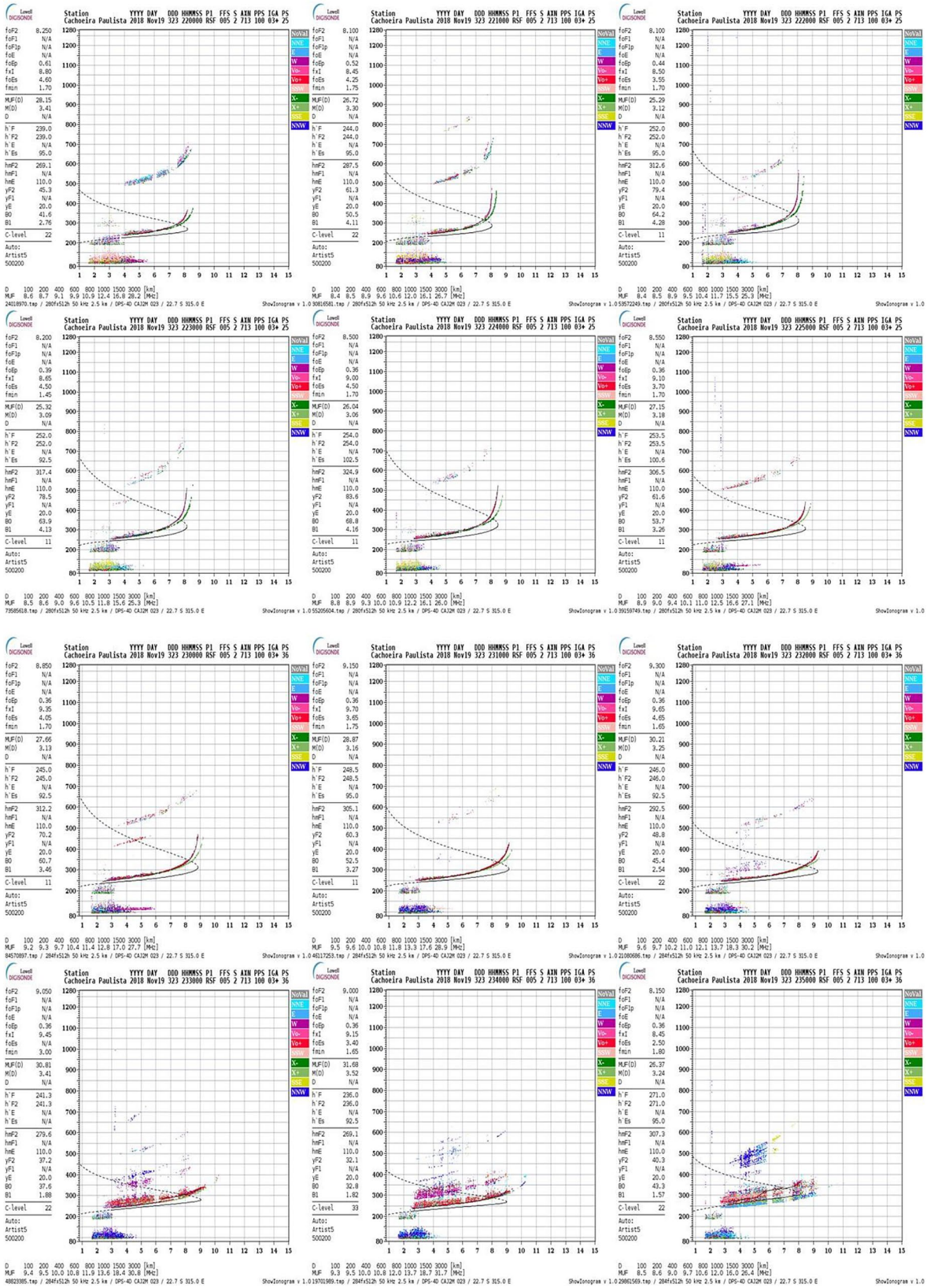

Figure A1. The Ionogram between 22:00 UT and 23:50 UT at Cachoeira Paulista (CP).

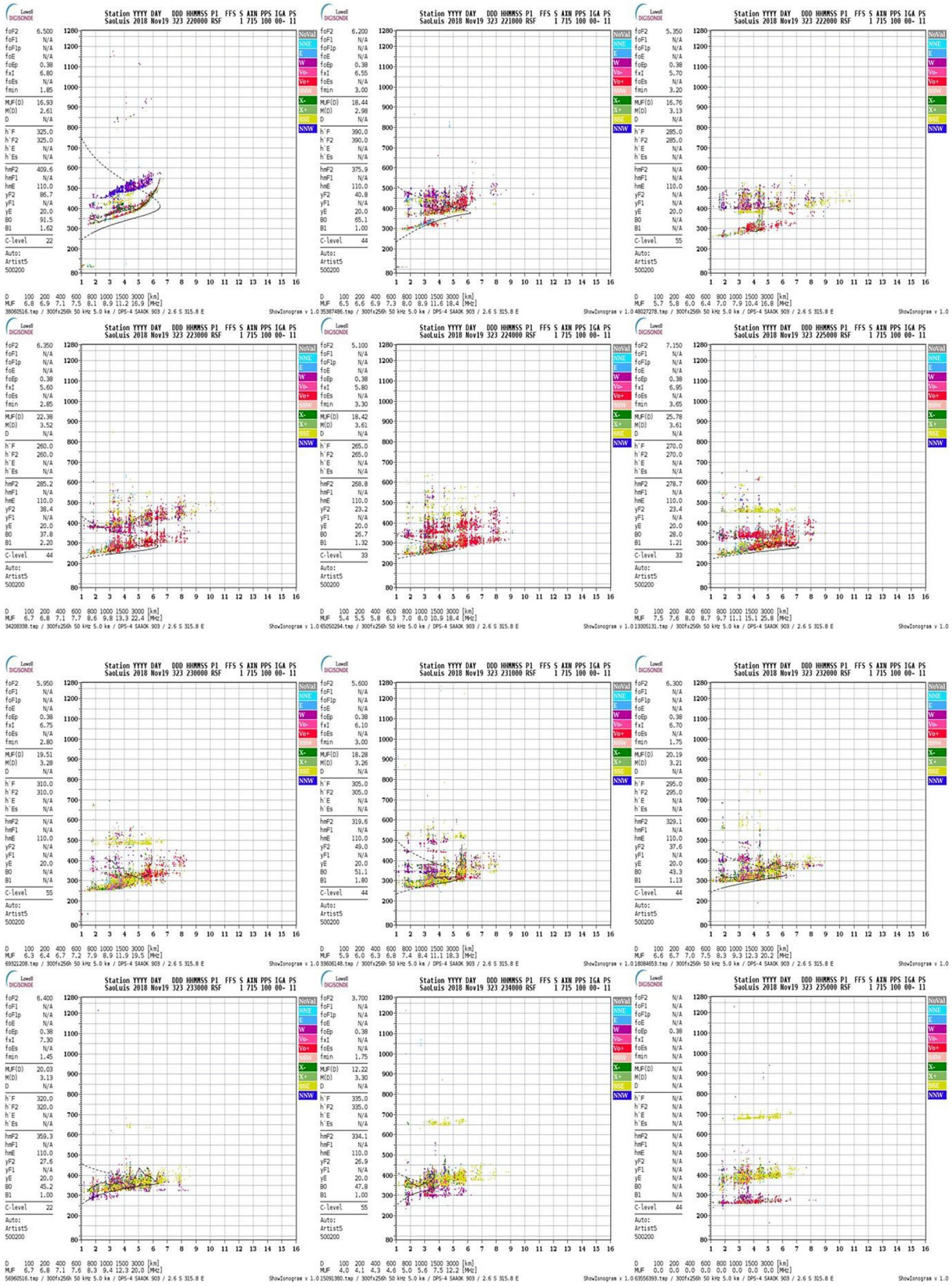

Figure A2. The ionogram between 22:00 UT and 23:50 UT at Sao Luis.

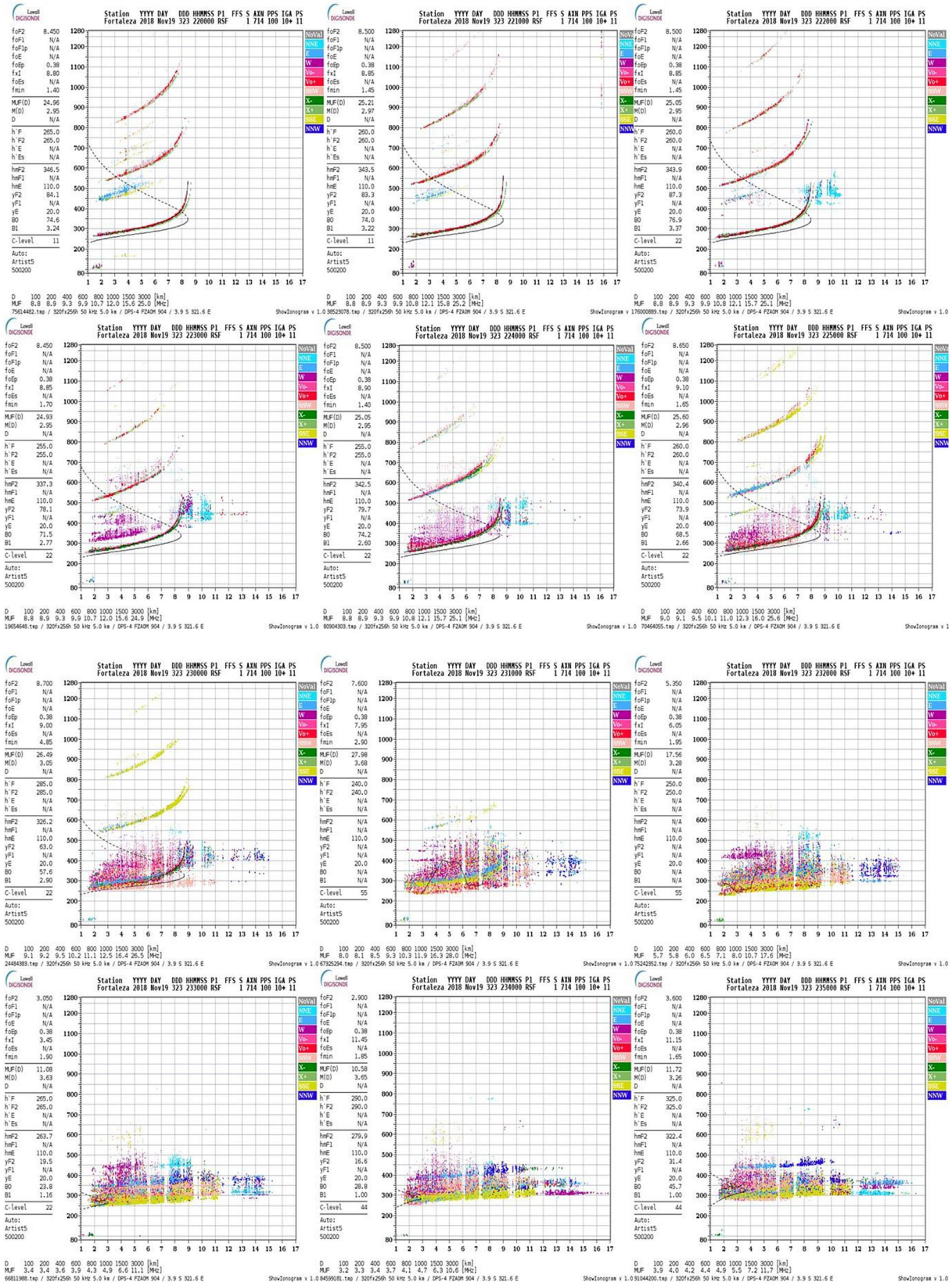

Figure A3. The Ionogram between 22:00 UT and 23:50 UT at Fortaleza.

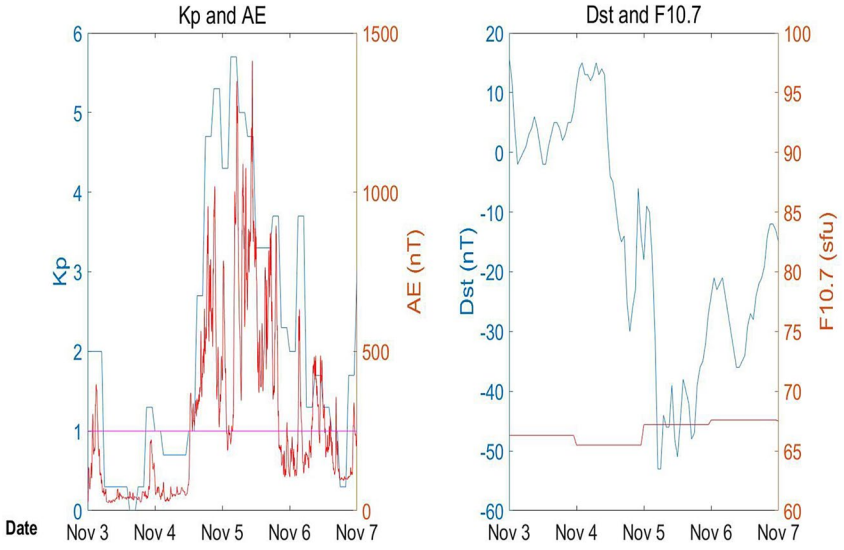

Figure A4. Temporal variation of Kp and AE, Dst and F10.7 between Nov 3 and 7 in 2018. The pink line stands for AE = 250 nT. AE, Auroral electrojet; Dst, Disturbance storm time.

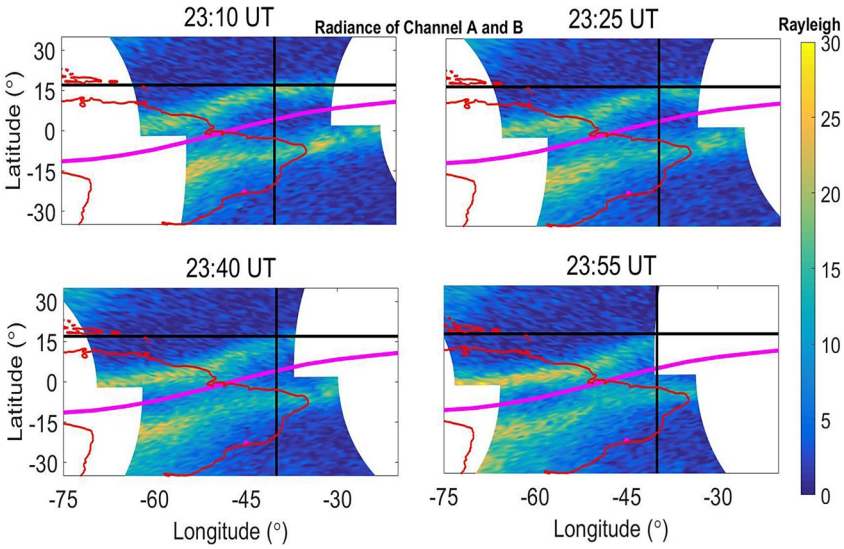

Figure A5. Same as Figure 4, but on November 4, 2018.

Data Availability Statement

The GOLD data are available from http://gold.cs.ucf.edu/. Digisonde data from Cachoeira Paulista is available at http://giro.uml.edu/didbase/scaled.php. The TEC data can be downloaded at http://landau.geo.cornell.edu/madrigal. The Auroral electrojet index data is from http://supermag.jhuapl.edu/. The TEC data can be downloaded http://millstonehill.haystack.mit.edu/.

Acknowledgments
This study is supported by NASA contract 80GSFC18C0061 to the University of Colorado. The authors thank the Instituto Nacional de Pesquisas Espaciais (INPE) in Brazil for making their Digisonde data from Cachoeira Paulista available through the Lowell GIRO Data Center. This work is also supported in part by NASA grants NNX15AB83G, NNX17AI42G, NNX16AH06G, 80NSSC19K0278, 80NSSC19K0835, 80NSSC20K0198 and 80NSSC17K0013. The National Center for Atmospheric Research is sponsored by the National Science Foundation. GPS TEC data products and access through the Madrigal distributed data system are provided to the community (http://www.openmadrigal.org) by the Massachusetts Instituition of Technology (MIT) under support from the U.S. NSF Grant AGS- 1952737. Data for the TEC processing is provided from the following organizations: UNAVCO, Scripps Orbits and Permanent Array Center, Instituto Brasileiro de Geografia e Estatistica, RAMSAC CORS of Instituto, Geografico Nacional de la Republica Argentina, Arecibo Observatory, Low-Latitude Ionospheric Sensor Network (LISN), Topcon Positioning Systems, Inc., Canadian High Arctic Ionospheric Network, Institute of Geology and Geophysics, Chinese Academy of Sciences, China Meteorology Administration, Centro di Ricerche Sismologiche, Systeme d'Observation du Niveau des Eaux Littorales (SONEL), RENAG: REseau NAtional GPS permanent, Geonet-the official source of geological hazard information for New Zealand, GNSS Reference Networks, Finnish Meteorological Institute, SWEPOS-Sweden, Hartebeesthoek Radio Astronomy Observatory, TrigNet Web Application, South Africa, Australian Space Weather Services, RETE INTEGRATA NAZIONALE GPS, Estonian Land Board, and Virginia Tech Center for Space Science and Engineering Research

References

Anderson, D. N., & Klobuchar, J. A. (1983). Modeling the total electron content observations above Ascension Island. *Journal of Geophysical Research*, *88*(A10), 8020–8024. https://doi.org/10.1029/JA088iA10p08020

Appleton, E. V. (1946). Two anomalies in the ionosphere. *Nature (London)*, *157*(3995), 691. https://doi.org/10.1038/157691a0

Balan, N., & Bailey, G. J. (1992). Latitudinal variations of nighttime enhancements in TEC: Solar and magnetic activity effects. *Advances in Space Research*, *12*(6), 219–222. https://doi.org/10.1016/0273-1177(92)90059-7

Balan, N., Bailey, G. J., Nair, R. B., & Titheridge, J. E. (1994). Nighttime enhancements in ionospheric electron content in the northern and southern hemisphere. *Journal of Atmospheric and Solar-Terrestrial Physics*, *56*(1), 67–79. https://doi.org/10.1016/0021-9169(94)90177-5

Balan, N., Rajesh, P. K., Sripathi, S., Tulasiram, S., Liu, J. Y., & Bailey, G. J. (2013). Modeling and observations of the north–south ionospheric asymmetry at low latitudes at long deep solar minimum. *Advances in Space Research*, *53*, 724–733. https://doi.org/10.1016/j.asr.2013.12.019

Balan, N., & Rao, P. B. (1987). Latitudinal variations of nighttime enhancements in total electron content. *Journal of Geophysical Research*, *92*, 3436–3440.

Basu, S., Basu, S., Huba, J., Krall, J., McDonald, S. E., Makela, J. J., et al. (2009). Day-to-day variability of the equatorial ionization anomaly and scintillations at dusk observed by GUVI and modeling by SAMI3. *Journal of Geophysical Research*, *114*, A04302. https://doi.org/10.1029/2008JA013899

Bellchambers, W. H., & Piggott, W. R. (1958). Ionospheric measurements made at Halley Bay. *Nature*, *182*, 1596–1597. https://doi.org/10.1038/1821596a0

Cai, X., Burns, A. G., Wang, W., Qian, L., Solomon, S. C., Eastes, R. W., et al. (2020a). The Two-Dimensional Evolution of Thermospheric ∑O/N 2 Response to Weak Geomagnetic Activity During Solar-Minimum Observed by GOLD. *Geophysical Research Letters*, *47*, e2020GL088838. https://doi.org/10.1029/2020gl088838

Cai, X., Burns, A. G., Wang, W., Coster, A., Qian, L., Liu, J., et al. (2020b). Comparison of GOLD nighttime measurements with total electron content: Preliminary results. *Journal of Geophysical Research: Space Physics*, *125*, e2019JA027767. https://doi.org/10.1029/2019ja027767

Chen, C. H., Huba, J. D., Saito, A., Lin, C. H., & Liu, J. Y. (2011). Theoretical study of the ionospheric Weddell Sea Anomaly using SAMI2. *Journal of Geophysical Research*, *116*, A04305. https://doi.org/10.1029/2010JA015573

Chen, C. H., Lin, C. H., Chang, L. C., Huba, J. D., Lin, J. T., Saito, A., & Liu, J. Y. (2013). Thermospheric tidal effects on the ionospheric midlatitude summer nighttime anomaly using SAMI3 and TIEGCM. *Journal of Geophysical Research: Space Physics*, *118*, 3836–3845. https://doi.org/10.1002/jgra.50340

Chen, J., & Lei, J. (2019). A simulation study on the latitudinal variations of ionospheric zonal electric fields under geomagnetically quiet conditions. *Journal of Geophysical Research: Space Physics*, *124*(2), 1444–1453. https://doi.org/10.1029/2018ja026174

Chen, Y., Liu, L., Le, H., Wan, W., & Zhang, H. (2015). N_mF_2 enhancement during ionospheric F_2 region nighttime: A statistical analysis based on COSMIC observations during the 2007–2009 solar minimum. *Journal of Geophysical Research: Space Physics*, *120*, 10083–10095. https://doi.org/10.1002/2015JA021652

Dang, T., Luan, X., Lei, J., Dou, X., & Wan, W. (2016). A numerical study of the interhemispheric asymmetry of the equatorial ionization anomaly in solstice at solar minimum. *Journal of Geophysical Research: Space Physics*, *121*, 9099–9110. https://doi.org/10.1002/2016JA023012

Davies, K., Anderson, D. N., Paul, A. K., Degenhardt, W., Hartmann, G. K., & Leitinger, R. (1979). Night-time increase in total electron content observed with the ATS6 radio beacon. *Journal of Geophysical Research*, *84*, 1536–1542. https://doi.org/10.1029/JA084iA04p01536

DeMajistre, R., Paxton, L. J., Morrison, D., Yee, J.-H., Goncharenko, L. P., & Christensen, A. B. (2004). Retrievals of nighttime electron density from Thermosphere Ionosphere Mesosphere Energetics and Dynamics (TIMED) mission Global Ultraviolet Imager (GUVI) measurements. *Journal of Geophysical Research*, *109*, A05305. https://doi.org/10.1029/2003JA010296

Eastes, R. W., McClintock, W. E., Burns, A. G., Anderson, D. N., Andersson, L., Aryal, S., et al. (2020). Initial Observations by the Global-scale Observations of the Limb and Disk (GOLD) mission. *Journal of Geophysical Research: Space Physics*, *125*, e2020JA027823. https://doi.org/10.1029/2020JA027823

Eastes, R. W., McClintock, W. E., Burns, A. G., Anderson, D. N., Andersson, L., Codrescu, M., et al. (2017). The Global-Scale Observations of the Limb and Disk (GOLD) mission. *Space Science Reviews*, *212*(1–2), 383–408. https://doi.org/10.1007/s11214-017-0392-2

Eastes, R. W., Solomon, S. C., Daniell, R. E., Anderson, D. N., Burns, A. G., England, S. L., et al. (2019). Global-scale observations of the equatorial ionization anomaly. *Geophysical Research Letters*, *46*, 9318–9326. https://doi.org/10.1029/2019GL084199

Eccles, J. V., St. Maurice, J. P., & Schunk, R. W. (2015). Mechanisms underlying the prereversal enhancement of the vertical plasma drift in the low-latitude ionosphere. *Journal of Geophysical Research: Space Physics*, *120*(6), 4950–4970. https://doi.org/10.1002/2014ja020664

Essex, E. A., & Klobuchar, J. A. (1980). Mid-latitude winter nighttime increases in the total electron content of the ionosphere. *Journal of Geophysical Research*, *85*, 6011–6020. https://doi.org/10.1029/JA085iA11p06011

Evans, J. V. (1965). Cause of the Midlatitude evening increase in f_0F_2. *Journal of Geophysical Research*, *70*, 1175–1185. https://doi.org/10.1029/JZ070i005p01175

Farelo, A. F., Herraiz, M., & Mikhailov, A. V. (2002). Global morphology of night-time NmF2 enhancements. *Annales Geophysicae*, *20*, 1795–1806. https://doi.org/10.5194/ANGEO-20-1795-2002

Finlay, C. C., Maus, S., Beggan, C. D., Bondar, T. N., Chambodut, A., Chernova, T. A., et al. (2010). International Geomagnetic Reference Field: The eleventh generation. *Geophysical Journal International*, *183*(3), 1216–1230. https://doi.org/10.1111/j.1365-246X.2010.04804.x

Galkin, I. A., Reinisch, B. W., Huang, X., & Bilitza, D. (2012). Assimilation of GIRO data into a real-time IRI. *Radio Science*, *47*, RS0L07. https://doi.org/10.1029/2011RS004952

He, M., Liu, L., Wan, W., Ning, B., Zhao, B., Wen, J., et al. (2009). A study of the Weddell Sea Anomaly observed by FORMOSAT-3/COSMIC. *Journal of Geophysical Research*, *114*, A12309. https://doi.org/10.1029/2009JA014175

Heelis, R. A., Lowell, J. K., & Spiro, R. W. (1982). A model of the high-latitude ionospheric convection pattern. *Journal of Geophysical Research*, *87*, 6339. https://doi.org/10.1029/ja087ia08p06339

Henderson, S. B., Swenson, C. M., Christensen, A. B., & Paxton, L. J. (2005). Morphology of the equatorial anomaly and equatorial plasma bubbles using image subspace analysis of Global Ultraviolet Imager data. *Journal of Geophysical Research*, *110*, A11306. https://doi.org/10.1029/2005JA011080

Huang, H., Lu, X., Liu, L., Wang, W., & Li, Q. (2018). Transition of interhemispheric asymmetry of equatorial ionization anomaly during solstices. *Journal of Geophysical Research: Space Physics*, *123*, 10283–10300. https://doi.org/10.1029/2018JA026055

Jiang, C., Deng, C., Yang, G., Liu, J., Zhu, P., Yokoyama, T., et al. (2016). Latitudinal variation of the specific local time of postmidnight enhancement peaks in F layer electron density at low latitudes: A case study. *Journal of Geophysics Research: Space Physics*, *121*(4), 3476–3483. https://doi.org/10.1002/2015JA022319

Karan, D. K., Daniell, R. E., England, S. L., Martinis, C. R., Eastes, R. W., Burns, A. G., & McClintock, W. E. (2020). First zonal drift velocity measurement of equatorial plasma bubbles (EPBs) from a geostationary orbit using GOLD data. *Journal of Geophysical Research: Space Physics*, *125*, e2020JA028173. https://doi.org/10.1029/2020ja028173

Kelley, M. C., Makela, J. J., Paxton, L. J., Kamalabadi, F., Comberiate, J. M., & Kil, H. (2003). First observations of plasma bubbles from space. *Geophysical Research Letters*, *30*(14), 1766. https://doi.org/10.1029/2003GL017301

Khadka, S. M., Valladares, C. E., Sheehan, R., & Gerrard, A. J. (2018). Effects of electric field and neutral wind on the asymmetry of equatorial ionization anomaly. *Radio Science*, *53*, 683–697. https://doi.org/10.1029/2017RS006428

Kil, H., DeMajistre, R., Paxton, L. J., & Zhang, Y. (2006). Nighttime F-region morphology in the low and middle latitudes seen from DMSP F15 and TIMED/GUVI. *Journal of Atmospheric and Solar-Terrestrial Physics*, *68*, 1672–1682. https://doi.org/10.1016/j.jastp.2006.05.024

Laskar, F. I., Eastes, R. W., Martinis, C. R., Daniell, R. E., Pedatella, N. M., Burns, A. G., et al. (2020). Early morning equatorial ionization anomaly from GOLD observations. *Journal of Geophysical Research: Space Physics*, *125*, e2019JA027487. https://doi.org/10.1029/2019ja027487

Le, H., Liu, L., Chen, Y., Zhang, H., & Wan, W. (2014). Modeling study of nighttime enhancements in F region electron density at low latitudes. *Journal of Geophysical Research: Space Physics*, *119*, 6648–6656. https://doi.org/10.1002/2013JA019295

Lei, J., Syndergaard, S., Burns, A. G., Solomon, S. C., Wang, W., Zeng, Z., et al. (2007). Comparison of COSMIC ionospheric measurements with ground-based observations and model predictions: Preliminary results. *Journal of Geophysical Research*, *112*, A07308. https://doi.org/10.1029/2006JA012240

Lei, J., Wang, W., Burns, A. G., Solomon, S. C., Richmond, A. D., Wiltberger, M., et al. (2008). Observations and simulations of the ionospheric and thermospheric response to the December 2006 geomagnetic storm: Initial phase. *Journal of Geophysical Research*, *113*, A01314. https://doi.org/10.1029/2007JA012807

Lin, C. H., Liu, J. Y., Fang, T. W., Chang, P. Y., Tsai, H. F., Chen, C. H., & Hsiao, C. C. (2007). Motions of the equatorial ionization anomaly crests imaged by FORMOSAT-3/COSMIC. *Geophysical Research Letters*, *34*, L19101. https://doi.org/10.1029/2007GL030741

Liu, L., Chen, Y., Le, H., Ning, B., Wan, W., Liu, J., & Hu, L. (2013). A case study of postmidnight enhancement in F-layer electron density over Sanya of China. *Journal of Geophysical Research: Space Physics*, *118*, 4640–4648. https://doi.org/10.1002/jgra.50422

Liu, J., Wang, W., Burns, A., Solomon, S. C., Zhang, S., Zhang, Y., & Huang, C. (2016). Relative importance of horizontal and vertical transports to the formation of ionospheric storm-enhanced density and polar tongue of ionization. *Journal of Geophysical Research: Space Physics*, *121*, 8121–8133. https://doi.org/10.1002/2016JA022882

Luan, X., Wang, W., Burns, A., Solomon, S. C., & Lei, J. (2008). Midlatitude nighttime enhancement in F region electron density from global COSMIC measurements under solar minimum winter condition. *Journal of Geophysical Research*, *113*, A09319. https://doi.org/10.1029/2008JA013063

Luan, X., Wang, P., Dou, X., & Liu, Y. C. M. (2015). Interhemispheric asymmetry of the equatorial ionization anomaly in solstices observed by COSMIC during 2007–2012. *Journal of Geophysical Research: Space Physics*, *120*, 3059–3073. https://doi.org/10.1002/2014JA020820

McDonald, S. E., Dymond, K. F., & Summers, M. E. (2008). Hemispheric asymmetries in the longitudinal structure of the low-latitude night time ionosphere. *Journal of Geophysical Research*, *113*, A08308. https://doi.org/10.1029/2007JA012876

McClintock, W. E., Eastes, R. W., Beland, S., Bryant, K. B., Burns, A. G., Correira, J., et al. (2020). Global-scale observations of the limb and disk mission implementation: 2. Observations, data pipeline, and level 1 data products. *Journal of Geophysical Research: Space Physics*, *125*, e2020JA027809. https://doi.org/10.1029/2020JA027809

Meléndez-Alvira, D. J., Meier, R. R., Picone, J. M., Feldman, P. D., & McLaughlin, B. M. (1999). Analysis of the oxygen nightglow measured by the Hopkins Ultraviolet Telescope: Implications for ionospheric partial radiative recombination rate coefficients. *Journal of Geophysical Research*, *104*, 14901–14913.

Mikhailov, A. V., Leschinkaya, T. Y., & Förster, M. (2000). Morphology of NmF2 nighttime increases in the Eurasian sector. *Annales Geophysicae*, *18*, 618–628. https://doi.org/10.1007/s00585-000-0618-5

Nicolls, M. J., Kelley, M. C., Vlasov, M. N., Sahai, Y., Chau, J. L., Hysell, D. L., et al. (2006). Observations and modeling of post-midnight uplifts near the magnetic equator. *Annales Geophysicae*, *24*, 1317–1331. https://doi.org/10.5194/angeo-24-1317-2006

Pavlov, A. V., & Pavlova, N. M. (2005). Mechanism of the post-midnight winter night-time enhancements in NmF2 over Millstone Hill during 14–17 January 1986. *Journal of Atmospheric and Solar-Terrestrial Physics*, *67*, 381–395. https://doi.org/10.1016/j.jastp.2004.11.004

Perna, L., Pezzopane, M., Zuccheretti, E., Fagundes, P. R., deJesus, R., Cabrera, M. A., & Ezquer, R. G. (2014). Unusual nighttime impulsive *fo*F2 enhancements at low latitudes: phenomenology and possible explanations. *Advances in Space Research*, *54*(3), 369–384. http://dx.doi.org/10.1016/j.asr.2013.05.014

Pezzopane, M., Fagundes, P. R., Ciraolo, L., Correia, E., Cabrera, M. A., & Ezquer, R. G. (2011). Unusual nighttime impulsive *fo*F2 enhancement below the southern anomaly crest under geomagnetically quiet conditions. *Journal of Geophysical Research*, *116*, A12314. https://doi.org/10.1029/2011JA016593

Rajesh, P. K., Liu, J. Y., Balan, N., Lin, C. H., Sun, Y. Y., & Pulinets, S. A. (2016). Morphology of midlatitude electron density enhancement using total electron content measurements. *Journal of Geophysical Research: Space Physics*, *121*, 1503–1517. https://doi.org/10.1002/2015JA022251

Rajesh, P. K., Liu, J. Y., Hsu, M. L., Lin, C. H., Oyama, K. I., & Paxton, L. J. (2011). Ionospheric electron content and NmF2 from nighttime OI 135.6 nm intensity. *Journal of Geophysical Research*, *116*, A02313. https://doi.org/10.1029/2010JA015686

Rama Rao, P. V. S., Gopi Krishna, S., Niranjan, K., & Prasad, D. S. V. V. D. (2006). Temporal and spatial variations in TEC using simultaneous measurements from Indian GPS network of receivers during the low solar activity period of 2004–2005. *Annales Geophysicae*, *24*, 1–4. https://doi.org/10.5194/angeo-24-3279-2006

Reinisch, B. W., & Galkin, I. A. (2011). Global ionospheric radio observatory (GIRO). *Earth, Planets and Space*, *63*, 377–381. https://doi.org/10.5047/eps.2011.03.001

Ren, Z., Wan, W., Liu, L., Le, H., & He, M. (2012). Simulated midlatitude summer nighttime anomaly in realistic geomagnetic fields. *Journal of Geophysical Research*, *117*, A03323. https://doi.org/10.1029/2011JA017010

Rideout, W., & Coster, A. (2006). Automated GPS processing for global total electron content data. *GPS Solutions*, *10*(3), 219–228. https://doi.org/10.1007/s10291-006-0029-5

Roble, R. G., Ridley, E. C., Richmond, A. D., & Dickinson, R. E. (1988). A coupled thermosphere/ionosphere general circulation model. *Geophysical Research Letters*, *15*(12), 1325–1328. https://doi.org/10.1029/gl015i012p01325

Schunk, R. W., & Nagy, A. F. (2009). *Ionospheres: Physics, plasma physics, and chemistry*. Cambridge, UK: Cambridge University Express.

Solomon, S. C., Qian, L., & Mannucci, A. J. (2018). Ionospheric electron content during solar cycle 23. *Journal of Geophysical Research: Space Physics*, *123*, 5223–5231. https://doi.org/10.1029/2018JA025464

Su, Y. Z., Bailey, G. J., & Balan, N. (1994). Night-time enhancements in TEC at equatorial anomaly latitudes. *Journal of Atmospheric and Solar-Terrestrial Physics*, *56*, 1619–1628. https://doi.org/10.1016/0021-9169(94)90091-4

Talaat, E. R., Yee, J.-H., Hsieh, S.-Y., Paxton, L. J., DeMajistre, R., Christensen, A. B., & Bilitza, D. (2013). The quiet nighttime low-latitude ionosphere as observed by TIMED/GUVI. *Advances in Space Research*, *51*(4), 661–676. https://doi.org/10.1016/j.asr.2012.11.012

Thampi, S., Balan, N., Lin, C., Liu, H., & Yamamoto, M. (2011). Midlatitude Summer Nighttime Anomaly (MSNA)—Observations and model simulations. *Annales Geophysicae*, *29*, 157–165. https://doi.org/10.5194/angeo-29-157-2011

Thomas, L. (1968). The f2-region equatorial anomaly during solstice periods at sunspot maximum. *Journal of Atmospheric and Terrestrial Physics*, *30*(9), 1631–1640. https://doi.org/10.1016/0021-9169(68)90011-1

Trivedi, R., Jain, S., Jain, A., & Gwal, A. K. (2013). Solar and magnetic control on night-time enhancement in TEC near the crest of the Equatorial Ionization Anomaly. *Advances in Space Research*, *51*, 61–68. https://doi.org/10.1016/j.asr.2012.08.016

Tulasi Ram, S., Su, S. Y., & Liu, C. H. (2009). FORMOSAT-3/COSMIC observations of seasonal and longitudinal variations of equatorial ionization anomaly and its interhemispheric asymmetry during the solar minimum period. *Journal of Geophysical Research*, *114*, A06311. https://doi.org/10.1029/2008JA013880

Wang, W., Lei, J., Burns, A. G., Wiltberger, M., Richmond, A. D., Solomon, S. C., et al. (2008). Ionospheric electric field variations during a geomagnetic storm simulated by a coupled magnetosphere ionosphere thermosphere (CMIT) model. *Geophysical Research Letters*, *35*, L18105. https://doi.org/10.1029/2008GL035155

Weimer, D. R. (2005). Improved ionospheric electrodynamic models and application to calculating Joule heating rates. *Journal of Geophysical Research*, *110*, A05306. https://doi.org/10.1029/2004ja010884

Zeng, Z., Burns, A., Wang, W., Lei, J., Solomon, S., Syndergaard, S., et al. (2008). Ionospheric annual asymmetry observed by the COSMIC radio occultation measurements and simulated by the TIEGCM. *Journal of Geophysical Research*, *113*, A07305. https://doi.org/10.1029/2007JA012897

Zhang, M. L., Wan, W., Liu, L., & Ning, B. (2009). Variability study of the crest-to-trough TEC ratio of the equatorial ionization anomaly around 120°E longitude. *Advances in Space Research*, *43*(11), 1762–1769. https://doi.org/10.1016/j.asr.2008.09.031

Zhang, Y., Liu, L., Chen, Y., Liu, J., You, Y., & Li, M. (2015). Nighttime electron density enhancements at middle and low latitudes in East Asia. *Science China Earth Sciences*, *58*(4), 551–561. https://doi.org/10.1007/s11430-014-4953-x

Zhao, B., Wan, W., Liu, L., Igarashi, K., Nakamura, M., Paxton, L. J., et al. (2008). Anomalous enhancement of ionospheric electron content in the Asian-Australian region during a geomagnetically quiet day. *Journal of Geophysical Research*, *113*, A11302. https://doi.org/10.1029/2007JA012987

Zhao, B., Wan, W., Liu, L., & Ren, Z. (2009). Characteristics of the ionospheric total electron content of the equatorial ionization anomaly in the Asian-Australian region during 1996–2004. *Annales Geophysicae*, *27*, 3861–3873. https://doi.org/10.5194/angeo-27-3861-2009

Zhong, J., Lei, J., Yue, X., Luan, X., & Dou, X. (2019). Middle-latitudinal band structure observed in the nighttime ionosphere. *Journal of Geophysical Research: Space Physics*, *124*, 5857–5873. https://doi.org/10.1029/2018JA026059